




TECHNICAL ARTICLE

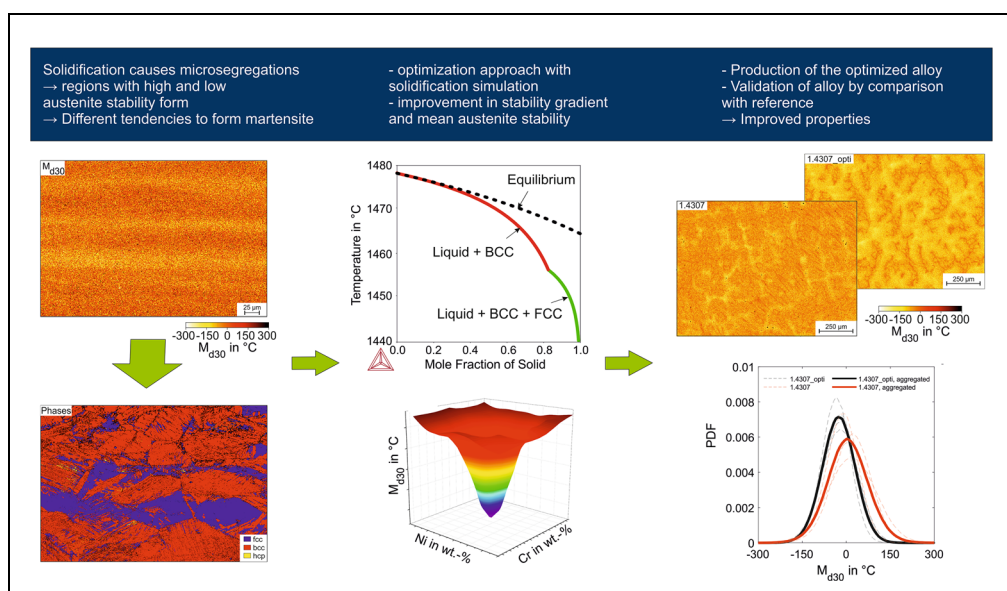
A New Approach to the Optimization of the Austenite Stability of Metastable Austenitic Stainless Steels

Aaron Berger , Gero Egels, Robert Fussik, Santiago Manuel Benito, and Sebastian Weber

Submitted: 29 August 2022 / Revised: 10 January 2023 / Accepted: 19 February 2023 / Published online: 23 March 2023

Austenitic steels used for components in high-pressure hydrogen storage systems in the automotive sector have to meet high requirements in terms of material properties and cost efficiency. The commonly used 1.4435/AISI 316L type steels fulfil the technological requirements but are comparatively expensive and resource-intensive. Lower alloyed steel grades are less costly, though prone to α -martensite formation and therefore sensitive to hydrogen embrittlement. Segregation-related fluctuations of the local element concentrations exert a strong impact on the austenite stability, thus controlling the segregation behavior can improve the austenite stability of lean alloyed steel grades, making them suitable for hydrogen applications. In this work, a novel approach for the optimization of alloy compositions with the aim of improving the homogeneity of the austenite stability is developed. The approach is based on combining automated Scheil–Gulliver solidification simulations with a multi-objective optimization algorithm. The solidification simulations provide information about the influence of the segregation profiles on the local austenite stability, which are then used to optimize the alloy composition automatically. The approach is exemplarily used for an optimization within the compositional range of 1.4307/AISI 304L. It is shown that a significant increase in the homogeneity of the austenite stability can be achieved solely by adjusting the global element concentrations, which has been validated experimentally.

Graphical Abstract



Keywords austenite stability, austenitic stainless steels, CALPHAD, hydrogen environment embrittlement, simulation, solidification, optimization

Aaron Berger, Gero Egels, Santiago Manuel Benito, and Sebastian Weber, Chair of Materials Technology, Ruhr-University Bochum, Universitätsstraße 150, 44801 Bochum, Germany; Robert Fussik, Chair of New Manufacturing Technologies and Materials, University of Wuppertal, Bahnhofstraße 15, 42651 Solingen, Germany. Contact e-mail: berger@wtech.rub.de.

1. Introduction

The stability of the austenitic face-centered cubic (fcc) phase against thermally activated or deformation-induced transformations to body-centered cubic (bcc) martensite is a crucial aspect for the suitability of austenitic stainless steels for hydrogen applications. fcc \rightarrow bcc transformations can drastically reduce the otherwise high resistance of CrNi-type austenitic stainless steels against hydrogen environment embrittlement (HEE) (Ref 1, 2). α -martensite is inherently more prone to hydrogen-induced cracking than austenite and also has a diffusivity for hydrogen atoms several orders of magnitude higher than the fcc-lattice of austenite (Ref 3-5). The latter allows a rapid accumulation of hydrogen atoms in critical sites like stress fields in front of notches or crack tips and thereby accelerates hydrogen-induced crack growth and fracture if α -martensite is present (Ref 6, 7). For this reason, HEE-resistant CrNi grades contain comparatively high amounts of Ni to provide sufficient phase stability at each position within the microstructure.

Commonly used approaches to quantify the austenite stability, and therefore also the resistance against HEE, are empirical equations for the calculation of the martensite start temperature (M_s) or the M_d -temperature, for thermally induced or deformation-induced phase transformations, respectively (Ref 2, 8, 9). Further, estimations of the austenite stability that use a thermodynamically calculated difference between the molar Gibbs energies of the fcc- and the bcc-phase, which is interpreted as a driving force for the phase transformation, can be found in the literature (Ref 10). Other authors use calculated or experimentally determined values of the stacking fault energy (SFE) as a measure for the austenite stability, as the SFE controls the formation of nucleation sites for α -martensite during plastic deformation (Ref 11-13).

In recent investigations, it has been proven that the fcc \rightarrow bcc transformation is not only dependent on the overall austenite stability, that can be estimated based on the global alloy composition by using one of the aforementioned approaches, but is strongly affected by segregation-related inhomogeneities of the austenite stability throughout the microstructure due to solidification (Ref 14-16). Segregation effects of the main alloying elements in CrNi-type steels entail local minima and maxima of the austenite stability. Local minima of the austenite stability are an effect of low alloyed regions in the microstructure and facilitate local hydrogen-induced cracking upon plastic deformation in hydrogen-containing atmospheres (Ref 17-19). In high alloyed steel grades, e.g., 1.4435, which is similar to AISI 316L, comparatively low alloyed regions provide a sufficiently high austenite stability to prevent deformation-induced phase transformations and H-induced crack formation. However, that is not the case in lower alloyed and more economical grades like 1.4307/AISI 304L, which may form H-induced cracks as a result of local segregation-related phase transformations under certain testing conditions (Ref 14).

By raising the alloy content of low-alloyed regions, the local minima of the austenite stability can be increased, resulting in a reduced overall tendency to form α -martensite and hydrogen-induced cracks.

The manifestation of microsegregations in austenitic steels depends to a large extent on the exact chemical composition of the melt. The reason for this is that the chemical composition

controls the sequence of the solidifying phases as well as their equilibrium compositions (Ref 20). It is therefore possible to tune an alloy composition in a way that reduces the degree of segregation, which may improve the resistance against HEE without adding significant amounts of alloying elements. Thus, an optimization of the segregation behavior of austenitic stainless steels like 1.4307, which have a lower overall alloy content compared to 1.4435, can possibly improve their hydrogen compatibility and allow a substitution of 1.4435 steels in hydrogen applications.

The present work describes a novel, simulation-based method to optimize the chemical composition of an austenitic stainless steel with the aim of achieving a high and homogeneously distributed austenite stability. The method combines solidification simulations based on the Scheil–Gulliver equation to predict element segregation with different calculation approaches for the austenite stability and a multi-objective optimization algorithm. In order to validate this approach, the description of the method is exemplary used for the optimization of a 1.4307 steel grade within its compositional limits.

2. Methods

In the context of this work, with the aid of the TC-Python Software Development Kit (SDK) of the Thermo-Calc Software, an approach to a new concept of alloy optimization is developed, focusing on the conception of the program as well as the optimization and validation of an alloy system. To that end, solidification simulations are automatically performed in the Scheil module of Thermo-Calc, from which data of the concentrations of the individual elements along the solidification profile are transferred to Python. These concentrations provide the basis for the calculation of the objective functions. In addition, laboratory-scale ingots are produced and characterized, to review the optimization as well as the optimized alloy, which has been developed in the optimization process.

2.1 Modeling

2.1.1 Thermodynamic Modeling. The thermodynamic simulations are carried out using the 2019b version of Thermo-Calc with the TCFE9 database. Thermo-Calc is integrated in the optimization scheme, which is programmed in Python version 3.8.0, importing the libraries *numpy*, *math* and *TC-Python*. The Scheil simulations start at a temperature of 2273 K. The check for a miscibility gap is not carried out and back diffusion of C was not allowed, due to restrictions in the *TC-Python* module. The alloy contents are varied within the ranges according to Table 1 in steps of 0.25 weight percent, which corresponds to a full factorial experimental design. After the calculation of the objective functions for each of these points, the optimized alloy has been identified regarding the criterion for an optimization on the Pareto-front.

2.1.2 Objective Functions. **2.1.2.1 Targets and Restrictions.** As previously described, depending on the chemical segregation degree, the global austenite stability might be an insufficient descriptor of the local resistance against HEE. Therefore, a local description is needed to optimize the resistance against phase transformations and HEE (Ref 14,

16, 21). Accordingly, the following targets have to be achieved:

- Maximize the overall level of the austenite stability
- Minimize the stability gradient

For an optimization, these targets are to be formulated as mathematical expressions, so-called objective functions. Thus, three different metrics are used to assess the austenite stability. The three mathematical expressions applied are the M_s -temperature according to Eichelmann and Hull (Ref 22),* the M_{d30} -temperature by Nohara et al.** (Ref 8), and an equation for calculating the stacking fault energy by Qui-Xun et al.† (Ref 23). This multi-objective optimization with three independent objective functions leads to an optimized system in all parameters on the Pareto-front (Ref 24, 25). The here used empirical formulations for the optimization are used because they represent the thermally induced and strain induced martensitic transformation. Furthermore, the usage of a formulation for the SFE enables the perspective of considering ϵ - as well as α -martensite, making the optimization procedure more precise.

The above-mentioned stability parameters are automatically calculated for every element concentration along the solidification curves simulated with the Scheil module. Each stability curve resulting from a solidification curve provides one minimum and one maximum value of each stability parameter. This enables the algorithm to compute the minimum austenite stability (M_{d30} -maximum, M_s -maximum, SFE-minimum) and the difference between maximum and minimum austenite stability (δM_{d30} , δM_s , δSFE). With this approach, it is possible to maximize the austenite stability by minimizing the stability gradient and shifting the mean austenite stability of the microstructure to higher values.

2.1.2.2 Multi-Objective Optimization. Since the problem at hand is a multi-objective optimization, a suitable formulation must be chosen to summarize the objective functions and to find an optimal solution on the Pareto-front. The approach in this work is based on the method of distance functions with standardization of distances (Eq. 1).

$$p[f(x)] = \sqrt[r]{\frac{|f_i(x) - y_i|}{y_i}} \quad (\text{Eq 1})$$

In this equation, $p[f(x)]$ is the objective function resulting from the objective functions $f_i(x)$ with the respective level of demand y_i . Furthermore, the exponent r has to be varied to assure that the summary objective function $p[f(x)]$ does not depend on a single objective function $f_i(x)$. The levels of demand are defined as described in Eq. 2.

$$y_i(f_i) = |f_i(x = x_{\text{maxima}})| + \left| \frac{f_i(x = x_{\text{maxima}}) - f_i(x = x_{\text{minima}})}{f_i(x = x_{\text{maxima}})} \right| \quad (\text{Eq 2})$$

$f_i(x = x_{\text{minima}})$ corresponds to the minimum of the objective function while the maximum is described by $f_i(x = x_{\text{maxima}})$.

* $M_s = 1305 - 2667 (C + N) - 41.7 Cr - 61.1 Ni - 27.8 Si - 33.3 Mn - 36.1 Mo$.
 ** $M_{d30} = 551 - 462 (C + N) - 9.2 Si - 8.1 Mn - 13.7 Cr - 29 (Ni + Cu) - 18.5 Mo - 68 Nb - 1.42 (\text{grainsize}[ASTM] - 8)$; The grain size will be neglected for the optimization.

† $SFE = SFE_{FE} + 1.59 Ni - 1.34 Mn + 0.06 Mn^2 - 1.75 Cr + 0.01 Cr^2 + 15.21 Mo - 5.59 Si - 60.69 (C + 1.2 N)^{0.5} + 26.27 (C + 1.2 N) * (Cr + Mo + Mn)^{0.5} + 0.61 (Ni * (Cr + Mn))^{0.5}$.

Table 1 Restrictions (upper and lower boundary conditions) in weight percent, based on the compositional range of 1.4307

	Cr	Ni	Mn	Si	Cu
Lower boundary	17.5	8	0	0	0
Upper boundary	19.5	10.5	2	1	1

This novel optimization design allows an optimization in an objective manner, since the quality of the solution by the method of distance functions strongly depends on the level of demand (Ref 25).

For the sake of achieving an optimized alloy composition within the compositional range of 1.4307 type steel, restrictions of the system 1.4307 are used, as shown in Table 1.

In addition, Fe is balanced and C is fixed at 0.03 weight percent. Trace elements like P, S and N are not considered. The optimization led to an optimized system, which will be characterized and validated in the following, by comparing the optimized system with a reference alloy out of the commercial heat of the austenitic stainless-steel grade 1.4307–X2CrNi18-9.

2.2 Experimental Validation

The optimized alloy was produced a 200 g ingot in a vacuum induction furnace by Leybold-Heraeus GmbH (Cologne, Germany) in a 500 mbar Ar atmosphere. The reference alloy 1.4307 was produced by Deutsche Edelstahlwerke Specialty Steel GmbH & Co. KG (Witten, Germany) by continuous casting and has been remelted under the same conditions as the optimized alloy. Chemical analysis of the investigated alloys is carried out by optical spark emission spectrometry (OES) using a QSG 750 by OBLF GmbH (Witten, Germany).

The ingots were solution-annealed at 1050 °C for 4 h in an argon atmosphere and quenched in water to reduce the δ -ferrite contents of the as-cast states.

For the investigation of the local element distributions and local stability parameters, specimens extending from the edge to the core of the ingots were metallographically prepared. The local element distributions were determined by means of energy-dispersive x-ray spectroscopy (EDS) using a MIRA 3 scanning electron microscope (SEM) by TESCAN ORSAY HOLDING, a.s. (Brno, Czech Republic), equipped with an X-Max 50 EDS detector by Oxford Instruments plc (Abingdon, England). The SEM was operated with an acceleration voltage of 20 kV and a working distance of 15 mm. Four EDS maps were recorded at different sites of each sample. The EDS maps cover an area of $1100 \times 820 \mu\text{m}$ each, and were recorded with a point-distance of $1 \mu\text{m}$ and a dwell time of 45 ms at each point. The acquired EDS data was subsequently quantified and exported as ASCII datasets. The ASCII datasets were used to calculate M_s , M_{d30} and the SFE for each datapoint of the EDS maps using MATLAB R2019b, resulting in two-dimensional distribution maps of the aforementioned parameters (Ref 26). As the local concentrations of the elements C and N cannot be quantitatively measured via EDS, the distribution of these elements was assumed to be constant with the concentration measured via OES.

The empirical equations for M_s , M_{d30} and SFE were previously used as objective functions for the optimization algorithm and are now adopted to assess the austenite stability distribution throughout the microstructure via EDS Mappings. In order to quantify the homogeneity of the austenite stability, the local values of the austenite stability measures were plotted as histograms. The sample mean μ , sample standard deviation σ , and mean absolute difference MAD were computed. The first parameter sheds light on the degree of the austenite stability and the other two, on its homogeneity. In particular, a lower mean value μ of M_s and M_{d30} implies higher stability, while a lower mean SFE values indicates a compromised austenite stability. Conversely, for all stability parameters, a low standard deviation and mean absolute difference point to a high homogeneity of the austenite stability—ultimately, both are dispersion descriptors of the selected measures. Equation 3, 4 and 5 display the measure definitions employed

$$\mu = \frac{1}{N} \sum_{i=1}^N X_i, \quad (\text{Eq 3})$$

$$\sigma = \sqrt{\frac{1}{N-1} \sum_{i=1}^N (X_i - \mu)^2}, \quad (\text{Eq 4})$$

$$\text{MAD} = \sum_{i=1}^n \sum_{j=1}^n f(x_i) f(x_j) |x_i - x_j|, \quad (\text{Eq 5})$$

where N is the number of elements in the mappings, X is a placeholder symbol for the stability metrics used, i.e., M_s , M_{d30} or SFE. $f(x_i)$ is the probability density normalized histogram value at x_i , such that $i = 1, 2, \dots, n$. In other words, n is the number of bins of the histogram $f(x)$ defined by the edges x . MAD complements σ as a dispersion measure because it is nothing other than the expected absolute property difference between any two randomly chosen points. Since $n \ll N$, Eq. (5) is much faster to compute than all the pairwise absolute differences in all maps.

3. Results and Discussion

3.1 Optimized Alloy

Table 2 contains the composition resulting from the optimization (target value) as well as the measured compositions of the ingots of the optimized alloy 1.4307_opti and the reference alloy 1.4307. The target composition reveals that the Ni content ran up against the upper boundary of the allowed range, while Cr and Mn contents ran against the lower boundary. The contents of Si and Cu show that the objective function has a local minimum within the allowed range.

The actual and the target composition of 1.4307_opti do not differ significantly. The produced 1.4307_opti ingot contains only small amounts of Mn, P, S, Mo and N due to impurities in the pre-alloys that were used. Accordingly, a high degree of agreement between the solidification behavior of the target and actual composition can be assumed. The reference alloy 1.4307 in comparison is alloyed with more Mn, Mo and N as well as less Ni.

3.2 Experimental Validation

An experimental validation is needed to verify the properties of the optimized alloy and the success of the optimization process. Figure 1 displays SEM images and the qualitative local distributions of the alloying elements of the investigated alloys in two of the recorded fields.

The EDS maps display an uneven distribution of the alloying elements resulting from the solidification. The element distributions of Cr and Ni show the most significant local variations in both materials, displayed with brighter or darker color shades. This can be related to the high global alloying quantities. Si shows smaller differences due to its low global quantity. The Mn mapping of the reference alloy evidences the presence of MnS inclusions, whereas in the optimized alloy, the local variations are minimal. Due to the presence and importance of Mn in technical alloys, the influence of Mn on the optimized system has to be pointed out (Fig. 2).

Figure 2 shows the influence of a variation of Mn on the segregation behavior of the alloying elements. Generally speaking, an increase of alloying elements which favor a primarily fcc-solidification (Ni, Mn, Cu, C, N) decrease the degree of segregation of one another (Ref 20, 27). Therefore, the alloying of Mn does not significantly influence the segregation behavior of the alloying elements, except for Cu. Nevertheless, Cu is only alloyed in small quantities. The increased segregation of Cu can therefore be seen as non-critical.

In both materials, minor contents of δ -ferrite appear to be present in regions with particularly high Cr and low Ni contents. In both alloys, an overall tendency for the enrichment of Ni in Cr-depleted regions is visible. The contrary segregation behavior of Cr and Ni is known from primarily ferritic solidifying austenitic steels and can also be considered here. The equilibrium concentration of Cr in a primarily solidifying bcc phase lies usually above the global Cr concentration of the melt, whereas the Ni concentration in the solidifying bcc phase is usually lower (Ref 28). Consequently, the melt is being depleted with Cr and enriched with Ni, which leads to the precipitation of fcc phase from the melt at some point, making the latter solidify Cr-poor and Ni-rich. Subsequent diffusion processes combined with bcc \rightarrow fcc transformations mitigate the resulting local composition gradients. Nonetheless, the contrary segregation tendencies persist in the solution-annealed condition. Pronounced contrary segregation effects do not necessarily result in strong gradients of the austenite stability; according to the equations of M_s and M_{d30} , all alloying elements contribute to a stabilization of the austenite. Contrary to the case of collective segregation effects of all alloying elements, contrary segregation tendencies can balance their local effects on the austenite stability to some extent and can therefore be regarded as beneficial for a homogeneous stability distribution. Figure 3 exemplary shows M_{d30} -maps of the investigated alloys (a) 1.4307 and (b) 1.4307_opti together with (c) histograms showing frequency distributions of the displayed data normalized by probability density.

While Fig. 3 (a) and (b) does not show obvious differences regarding the mean M_{d30} value as well as the homogeneity of M_{d30} , the histograms reveal improvements of both these properties in case of 1.4307_opti. The mean value of M_{d30} in alloy 1.4307_opti is shifted toward lower temperatures, indicating a more stable austenite on average. Also, the histogram shows a narrower profile, which means that the standard deviation will be smaller and thus the distribution of the

Table 2 Target and measured composition of the optimized alloy in wt.%. As a reference, the composition of the reference material is shown as well

	C	Si	Mn	P	S	Cr	Ni	Mo	Cu	N
Target value	0.03	0.5	0	0 (fixed)	0	17.5	10.5	0 (fixed)	0.75	0 (fixed)
1.4307_opti	0.012	0.519	0.058	0.01	0.004	17.12	10.2	0.018	0.78	0.008
1.4307	0.021	0.671	1.949	0.03	0.028	17.93	8.54	0.3	0.594	0.04

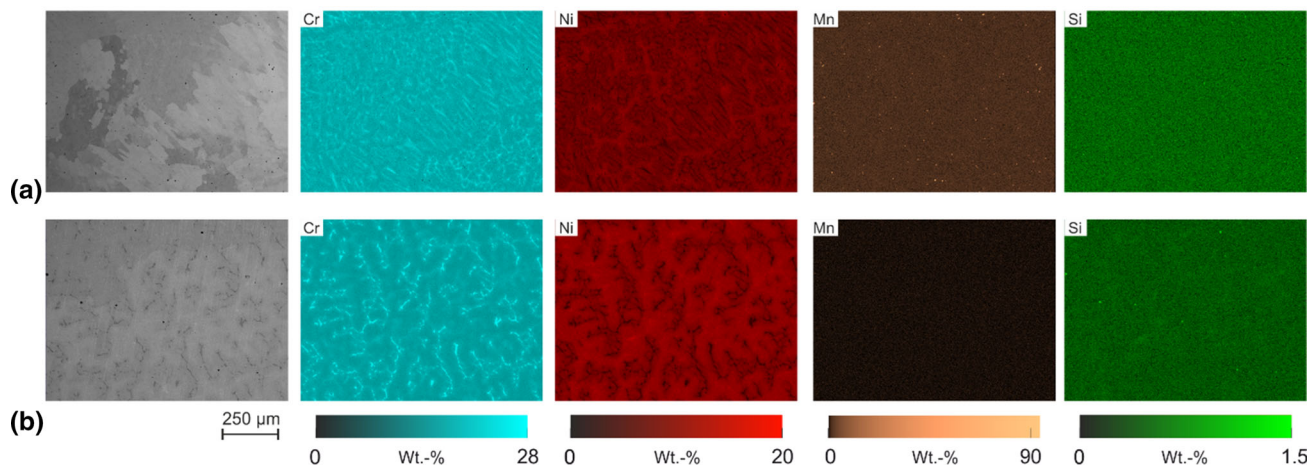


Fig. 1 Exemplary SEM images and qualitative local distributions of alloying elements in (a) 1.4307 and (b) 1.4307_opti

austenite stability is more homogeneous. A narrower histogram of a stability parameter which is shifted to a lower temperature indicates a higher, more homogeneous austenite stability.

In the same fashion as in Fig. 3 (c), Fig. 4 presents the probability density distributions of M_s , M_{d30} and the SFE for the alloys 1.4307 and 1.4307_opti. Note that fine lines correspond to the individual specimens #1-#4 and broad lines to their aggregation. Table 3, on the other hand, provides their mean values μ , their standard deviations σ , and mean absolute differences MAD, together with a relative difference calculation. Note that while the M_s and M_{d30} temperatures are presented in °C, for the computation of the relative differences between reference and optimized alloys the absolute temperature was used.

The presented data allow a comparison of the austenite stability in different locations of each ingot. It shows that there is some scattering between the data from different sites that were investigated. Scattering of μ can be explained by macrosegregation effects in the ingots, whereas the scattering of σ and MAD is most probably a result of local differences in the cooling conditions during solidification. The cooling rate especially influences the dendrite arm spacing, which defines the length scale of segregation structures (Ref 29). The smaller the length scale of the segregation structures, the faster homogenization can occur during solution annealing. Therefore, sites with a small initial dendrite arm spacing can be assumed to have a more homogeneous distribution of the austenite stability in the annealed state.

Overall tendencies and differences between the two considered alloys can be evaluated best by comparing the probability density distributions (Fig. 4) and the corresponding sample parameters (Table 3) of the aggregated data of each alloy. The

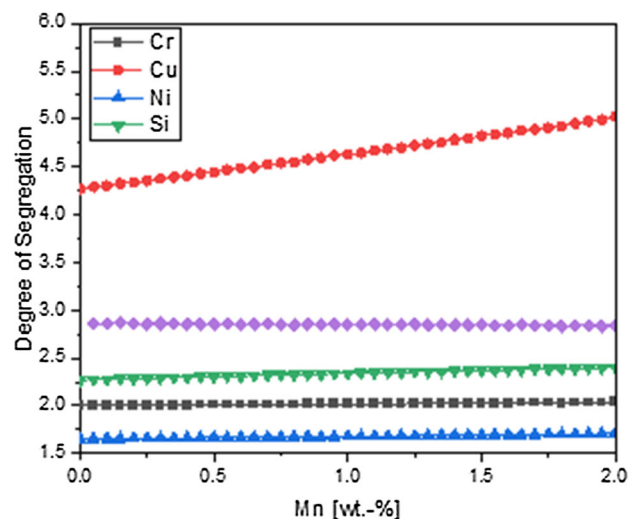


Fig. 2 Exemplary SEM images and qualitative local distributions of alloying elements in (a) 1.4307 and (b) 1.4307_opti

mean values of the M_{d30} temperature and the SFE indicate a higher mean austenite stability of the optimized alloy 1.4307_opti. In contrast, the M_s temperature shows the opposite tendency. M_{d30} of the steel 1.4307_opti is 31.3 °C lower, representing an improvement of 11.2%, while M_s is 73.5 °C higher compared to the steel 1.4307, indicating a 112.8% stability decrease. The divergent trends of M_s and M_{d30} can be mainly attributed to the contribution of the interstitial alloying elements C and N. These elements are considered to have a significantly greater influence on M_s than on M_{d30} (Ref 8, 22,

30). The much higher content of these elements in steel 1.4307 is therefore more evident in M_s than in M_{d30} . This indicates that the M_s temperature might not be suitable for the validation by EDS, which explains the decrease of the mean M_s in the optimized alloy.

As described above, not only the average austenite stability, but also its homogeneity, controls the actual transformation tendency of the austenite, as local stability minima provide favorable sites for martensite formation. For all three parameters describing the austenite stability, the sample standard deviation and mean absolute difference of the aggregated data indicates an improved homogeneity of the austenite stability in the optimized alloy 1.4307_opti. For instance, the expected absolute M_{d30} difference between any two points is 82.9 and 63.5 °C for the reference and optimized alloys, respectively. The relative improvements in terms of the M_s and M_{d30} temperatures are around 20%, while the SFE presents a homogeneity enhancement of 7.4%.

The mean M_{d30} as well as the mean M_s temperature of the steel 1.4307_opti lies well below room temperature and feature improved homogeneities. These factors indicate a reduced tendency to form martensite upon straining at room temperature, compared to the reference steel 1.4307. Moreover, the increased SFE can be considered to contribute to a more homogeneous deformation behavior and the provision of a lower number of nucleation sites for α -martensite due to less ϵ -martensite (Ref 31). The lower number of nucleation sites for martensite comes through the decreased σ in combination with an increased μ . As pointed out by Noh et al. (Ref 30), a SFE of 20 mJ/m² can be considered as a threshold for the formation of α -martensite. If now more regions in an alloy are locally below a SFE of 20 mJ/m², more nucleations sites for martensites and even more martensite will form. Therefore, the alloy 1.4307_opti can be considered as more resistant against the formation of nucleation sites.

Therefore, the steel 1.4307_opti proves the effectiveness of the implemented optimization approach for the design of a steel with an improved resistance against hydrogen embrittlement, which was the overarching aim. However, future studies have to investigate the mechanical properties of the optimized steel with and without influences of hydrogen. Additionally, some aspects of the optimization procedure are supposed to provide room for further improvement.

3.3 Optimization Strategy

An essential part of this work was the development of a suitable optimization approach. Every optimization approach consists of a fitting analysis model, purposeful objective functions and an appropriate optimization strategy. The optimization is based on the analysis model, in this case the Scheil module. The validity of this model is well documented in the literature and known to be suitable for the calculations that were carried out in the framework of the optimization process (Ref 32, 33). However, the peculiarities of the interstitial elements C and N could not be considered optimally, as these elements could not be defined as “fast diffusing components” because of limitations in the *TC-Python* module, that existed at the time the simulations were performed. The segregation of C and N is therefore assumed to be overestimated in the simulations which, however, could not be proven as these elements cannot be quantified in the EDS measurements.

Besides the analysis model, the optimization depends essentially on the selected objective functions (Ref 34). The objective functions are developed as derivations of stability parameters, which quantify the austenite stability (Ref 8, 22, 23). Consequently, the predictive power of the objective functions depends on the meaningfulness of the stability parameters. Even though considering stability parameters alone is not a sufficient prerequisite for resistance to hydrogen embrittlement, steels with high austenite stability nevertheless exhibit lower susceptibility to hydrogen embrittlement. This renders the approach presented here suitable for the optimization of austenitic steels for the use in hydrogen atmospheres.

The equations of the M_s and M_{d30} temperatures consider a linear influence of the alloying elements on the resulting stability parameter. This disables a consideration of interactions of the alloying elements. Another issue is the allowed alloying range of these stability parameters. King and Larbalestier (Ref 35) restrict the usable range of the M_s temperature, whereas the influence of Cr is considered too high and the influence of Ni is considered too low in the two investigated alloys. This effect is amplified in the higher alloyed regions in the solidification simulations and in the EDS mappings. The M_s temperature should therefore not be used as an exact number, but can be used for a qualitative comparison of the alloy systems.

Both the linear influence and the absence of interactions, as well as the limited alloying range, can be avoided by using the

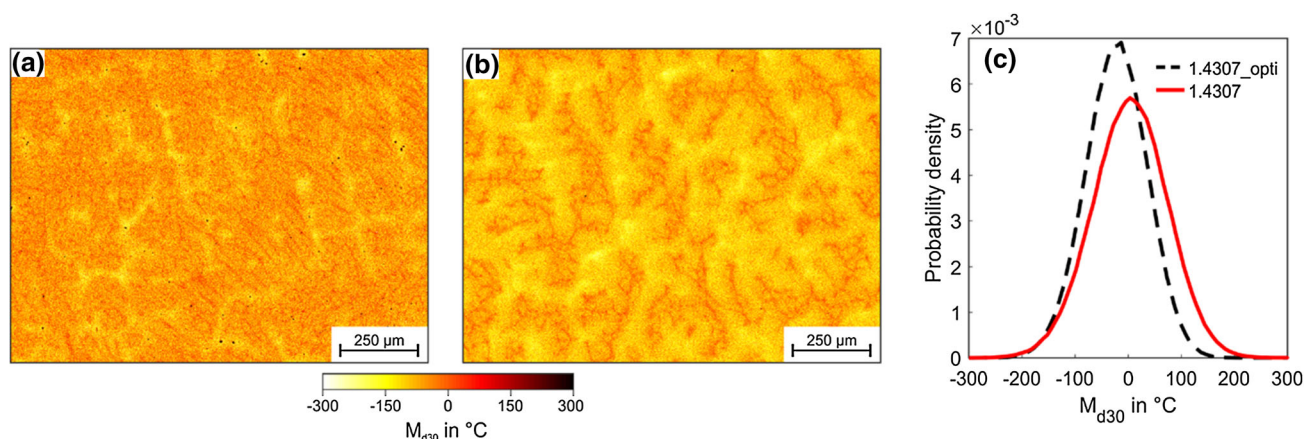


Fig. 3 Local distribution of M_{d30} for (a) 1.4307 and (b) 1.4307_opti calculated from quantified EDS datasets shown in Fig. 3. (c) shows the frequency distributions of M_{d30} in (a) and (b)

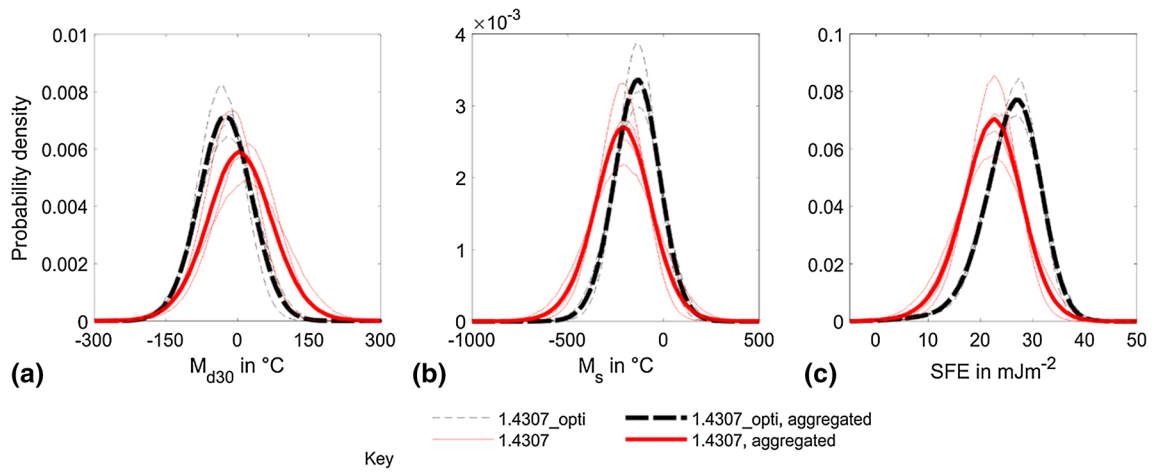


Fig. 4 Histograms of (a) M_{d30} , (b) M_s and (c) SFE. The fine lines represent the individual distributions of each measured field (1–4 for each alloy), while the broad lines correspond to their aggregation

Table 3 Parameters μ and σ of normal distributions fitted to datasets of M_s , M_{d30} , SFE calculated from EDS data

Dataset	M_{d30} [°C]			M_s [°C]			SFE [mJm^{-2}]		
	μ	σ	MAD	μ	σ	MAD	μ	σ	MAD
1.4307 #1	16.7	82.9	93.2	− 212.3	186.3	209.4	21.8	7.1	7.9
1.4307 #2	3.4	71.1	79.9	− 213.1	159.7	179.0	21.9	6.2	6.9
1.4307 #3	− 14.5	55.9	62.4	− 219.6	124.7	138.9	22.2	4.9	5.4
1.4307 #4	16.7	66.2	74.0	− 208.2	146.5	163.1	22.4	5.7	6.3
1.4307 #1–4	5.6	70.8	79.2	− 213.3	156.0	173.6	22.1	6.0	6.7
1.4307_opti #1	− 34.8	48.9	55.0	− 139.3	104.0	116.9	25.8	5.2	5.7
1.4307_opti #2	− 23.1	55.0	61.99	− 141.3	118.4	113.3	25.9	5.4	6.0
1.4307_opti #3	− 22.6	61.8	69.7	− 140.2	133.7	150.7	25.8	5.9	6.5
1.4307_opti #4	− 22.5	58.0	65.4	− 138.3	125.1	140.9	26.1	6.0	6.5
1.4307_opti #1–4	− 25.7	56.4	63.5	− 139.8	120.8	135.7	25.9	5.6	6.2
Rel. improvement in %	11.2	20.5	19.9	− 122.8	22.5	21.8	17.2	6.2	7.4

High importance values are given in bold

SFE formula (Ref 23). However, when using the empirical formula to calculate the SFE, attention must be paid to nonlinearity, since the minima and maxima of the function do not necessarily have exist in the areas that solidified first or last.

Overall, it must also be considered that the austenite stability was also determined for ferritic bcc phase solidifying from the melt. Since it is actually physically incorrect to calculate M_s and M_{d30} for ferrite, the usage of a Ni-equivalent might be a better alternative (Ref 36). On the other hand, especially the M_{d30} is well known for its significant correlation with the resistance against hydrogen environment embrittlement, which makes M_{d30} a meaningful parameter in the context of this study (Ref 2, 3, 14).

The method of distance functions was used as the optimization strategy in this study, as each objective function was supposed to be considered equally. Also, the method was normalized by relative distances with the weights not being predefined, but a result from the values of the objective functions. This is contrasted with the fact that the method of restriction-oriented transformation is considered the best method for Pareto optimization (Ref 34). This method is based on the formulation of a main objective and secondary objectives. Secondary objectives are seen only as constraints

that define the limits of the optimization. The formulation of a single main objective function is not possible in this case, because all objective functions, and stability parameters, respectively, represent an important parameter and point to different aspects of the phase transformation and therefore HEE. In particular, the quality of the stability parameters and thus of the functions is difficult to evaluate, which is why this method should not be used here. As the here used optimization strategy is independent of a single objective function, it is considered more suitable for the described application (Ref 25).

The considered optimization scheme has the goal to achieve a homogeneous and sufficient stable primary microstructure regarding the empirical formulations. Nevertheless, the secondary microstructure determines the characteristics and properties of a material or alloy, respectively. The secondary microstructure is determined by the primary microstructure due to the casting process and the secondary manufacturing processes like rolling or casting. Therefore, the primary microstructure plays a significant role for the secondary microstructure (Ref 37). If the secondary process is now considered as equal for both the optimized and conventional 1.4307, the optimized alloy will again show improved homogeneity regarding the stability parameters considered.

4. Summary

In this work, a novel approach for the optimization of austenitic stainless steel was implemented and validated. The presented approach incorporates an automated optimization strategy, which targets material properties, that are strongly influenced by segregation effects of the alloying elements. The following conclusions can be drawn from the investigations:

- By coupling Scheil–Gulliver solidification simulations with optimization functions, the chemical composition can be optimized to improve the overall austenite stability.
- Empirical equations describing the austenite stability are suited to serve as objective functions for multi-objective optimization strategies.
- The conceived optimization approach was successfully used to achieve an improved austenite stability within the alloying range of the steel 1.4307, which was proved by assessing local austenite stability distributions in laboratory-scale ingots.

In future attempts to develop novel alloys with optimized properties, the presented approach can be used beyond standardized compositional ranges, by shifting boundary conditions and adding more elements. By employing different objective functions, the approach can also be adapted to pursue the optimization of other material properties, e.g., corrosion resistance, or a combination of different properties. Upcoming studies will also investigate the here presented alloy 1.4307_opti in tensile tests in air and H₂-atmosphere. These tests will prove the improved properties of the optimized alloy and will validate the optimization procedure.

Acknowledgments

This work was supported by the Deutsche Forschungsgemeinschaft [Project-Nr. WE 4436/7-1].

Funding

Open Access funding enabled and organized by Projekt DEAL.

Open Access

This article is licensed under a Creative Commons Attribution 4.0 International License, which permits use, sharing, adaptation, distribution and reproduction in any medium or format, as long as you give appropriate credit to the original author(s) and the source, provide a link to the Creative Commons licence, and indicate if changes were made. The images or other third party material in this article are included in the article's Creative Commons licence, unless indicated otherwise in a credit line to the material. If material is not included in the article's Creative Commons licence and your intended use is not permitted by statutory regulation or exceeds the permitted use, you will need to obtain permission directly from the copyright holder. To view a copy of this licence, visit <http://creativecommons.org/licenses/by/4.0/>.

References

1. L. Zhang, M. Wen, M. Imade, S. Fukuyama, and K. Yokogawa, Effect of Nickel Equivalent on Hydrogen Gas Embrittlement of Austenitic Stainless Steels Based on type 316 at Low Temperatures, *Acta Mater.*, 2008, **56**, p 3414–3421. <https://doi.org/10.1016/j.actamat.2008.03.022>
2. C. Izawa, S. Wagner, M. Deutges, M. Martín, S. Weber, R. Pargeter, T. Michler, H.-H. Uchida, R. Gemma, and A. Pundt, Relationship Between Hydrogen Embrittlement and Md30 Temperature: Prediction of Low-Nickel Austenitic Stainless Steel's Resistance, *Int. J. Hydrog. Energy*, 2019, **44**, p 25064–25075. <https://doi.org/10.1016/j.ijhydene.2019.07.179>
3. M. Martin, S. Weber, C. Izawa, S. Wagner, A. Pundt, and W. Theisen, Influence of Machining-Induced Martensite on Hydrogen-Assisted Fracture of AISI Type 304 Austenitic Stainless Steel, *Int. J. Hydrog. Energy*, 2011, **36**, p 11195–11206. <https://doi.org/10.1016/j.ijhydene.2011.05.133>
4. C.S. Marchi, Hydrogen Embrittlement of Stainless Steels and Their Welds, *Gaseous Hydrogen Embrittlement of Materials in Energy Technologies*. Elsevier, Netherlands, 2012, p 592–623
5. B.S. Kumar, V. Kain, M. Singh, and B. Vishwanadh, Influence of Hydrogen on Mechanical Properties and Fracture of Tempered 13 wt% Cr Martensitic Stainless Steel, *Mater. Sci. Eng. A*, 2017, **700**, p 140–151. <https://doi.org/10.1016/j.msea.2017.05.086>
6. Y. Wang, X. Li, D. Dou, L. Shen, and J. Gong, FE analysis of Hydrogen Diffusion Around a Crack Tip in an Austenitic Stainless Steel, *Int. J. Hydrog. Energy*, 2016, **41**, p 6053–6063. <https://doi.org/10.1016/j.ijhydene.2016.03.003>
7. X. Sun, J. Xu, and Y. Li, Hydrogen Permeation Behavior in Metastable Austenitic Stainless Steels 321 and 304, *Acta Metall.*, 1989, **37**, p 2171–2176. [https://doi.org/10.1016/0001-6160\(89\)90142-9](https://doi.org/10.1016/0001-6160(89)90142-9)
8. K. Nohara, Y. Ono, and N. Ohashi, Composition and Grain Size Dependencies of Strain-induced Martensitic Transformation in Metastable Austenitic Stainless Steels, *Tetsu-to-Hagane*, 1977, **63**, p 772–782. https://doi.org/10.2355/tetsutohagane1955.63.5_772
9. K.W. Andrews, Empirical Formulae for the Calculation of Some Transformation Temperatures, *J. Iron Steel Inst.*, 1965, **203**, p 721–727.
10. M. Martin, S. Weber, and W. Theisen, A thermodynamic Approach for the Development of Austenitic Steels with a High Resistance to Hydrogen Gas Embrittlement, *Int. J. Hydrog. Energy*, 2013, **38**, p 14887–14895. <https://doi.org/10.1016/j.ijhydene.2013.08.133>
11. K. Sato, M. Ichinose, Y. Hirotsu, and Y. Inoue, Effects of Deformation Induced Phase Transformation and Twinning on the Mechanical Properties of Austenitic Fe-Mn-Al Alloys, *ISIJ Int.*, 1989, **29**, p 868–877. <https://doi.org/10.2355/isijinternational.29.868>
12. C. Ullrich, R. Eckner, L. Krüger, S. Martin, V. Klemm, and D. Rafaja, Interplay of Microstructure Defects in Austenitic Steel with Medium Stacking Fault Energy, *Mater. Sci. Eng. A*, 2016, **649**, p 390–399. <https://doi.org/10.1016/j.msea.2015.10.021>
13. J. Talonen and H. Hänninen, Formation of Shear Bands and Strain-Induced Martensite During Plastic Deformation of Metastable Austenitic Stainless Steels, *Acta Mater.*, 2007, **55**, p 6108–6118. <https://doi.org/10.1016/j.actamat.2007.07.015>
14. G. Egels, L. Mujica Roncery, R. Fussik, W. Theisen, and S. Weber, Impact of Chemical Inhomogeneities on Local Material Properties and Hydrogen Environment Embrittlement in AISI 304L Steels, *Int. J. Hydrog. Energy*, 2018, **43**, p 5206–5216. <https://doi.org/10.1016/j.ijhydene.2018.01.062>
15. R. Fussik, G. Egels, W. Theisen, and S. Weber, Investigation of the Local Austenite Stability Related to Hydrogen Environment Embrittlement of Austenitic Stainless Steels, *Mater. Sci. Forum*, 2018, **941**, p 263–268. <https://doi.org/10.4028/www.scientific.net/MSF.941.263>
16. R. Fussik and S. Weber, Local Microstructural Stability and Hydrogen Embrittlement of Iron-Base FCC Alloys, *J. Mater. Sci. Eng. A*, 2016, **6**, p 243–253. <https://doi.org/10.17265/2161-6213/2016.9-10.002>
17. T. Michler, Y. Lee, R.P. Gangloff, and J. Naumann, Influence of Macro Segregation on Hydrogen Environment Embrittlement of SUS 316L Stainless Steel, *Int. J. Hydrog. Energy*, 2009, **34**, p 3201–3209. <https://doi.org/10.1016/j.ijhydene.2009.02.015>

18. R.Q. Zhou, W.L. Sun, and Y.T. Jia, Study on Segregation and Homogenization Treatment of Cast 316L Stainless Steel, *Trans. Mater. Heat Treat.*, 2017, **38**, p 106–111.
19. F. Sadeghi, T. Zargar, J.W. Kim, Y.-U. Heo, J.S. Lee, and C.H. Yim, The Effect of Ni Depletion on Athermal Martensitic Transformation in 304 Austenitic Stainless Steel, *Mater. Charact.*, 2021, **175**, p 111063. <https://doi.org/10.1016/j.matchar.2021.111063>
20. N. Suutala, T. Takalo, and T. Moision, Ferritic-Austenitic Solidification Mode in Austenitic Stainless Steel Welds, *Metall. Trans.*, 1980, **11**, p 717–725. <https://doi.org/10.1007/BF02661201>
21. J. Man, I. Kuběna, M. Smaga, O. Man, A. Järvenpää, A. Weidner, Z. Chlup, and J. Polák, Microstructural Changes During Deformation of AISI 300 Grade Austenitic Stainless Steels: Impact of Chemical Heterogeneity, *Proc. Struct. Integr.*, 2016, **2**, p 2299–2306. <https://doi.org/10.1016/j.prostr.2016.06.288>
22. G.H. Eichelmann and F.C. Hull, The Effect of Composition on the Temperature of Spontaneous Transformation of Austenitic to Martensitic in 18–8 Stainless Steel, *Trans. ASM*, 1953, **45**, p 77–104.
23. Q.-X. Dai, A.-D. Wang, X.-N. Cheng, and X.-M. Luo, Stacking Fault Energy of Cryogenic Austenitic Steels, *Chin. Phys.*, 2002, **11**, p 596–600. <https://doi.org/10.1088/1009-1963/11/6/315>
24. T. Tusar and B. Filipic, Visualization of Pareto Front Approximations in Evolutionary Multiobjective Optimization: A Critical Review and the Prosection Method, *IEEE Trans. Evol. Comput.*, 2015, **19**, p 225–245. <https://doi.org/10.1109/TEVC.2014.2313407>
25. I.Y. Kim and O.L. de Weck, Adaptive Weighted Sum Method for Multiobjective Optimization: A New Method for Pareto Front Generation, *Struct. Multidisc. Optim.*, 2006, **31**, p 105–116. <https://doi.org/10.1007/s00158-005-0557-6>
26. R. Fussik and S. Weber, Derivation of Property Distribution Images from Microstructural Analyses of X2CrNi18-9 with Regard to Hydrogen Embrittlement, *Practic. Metallograph.*, 2018, **55**, p 387–399. <https://doi.org/10.3139/147.110522>
27. H.-J. Eckstein, *Korrosionsbeständige Stähle*, Deutscher Verlag für Grundstoffindustrie publisher, Leipzig, 1990
28. H.W. Kerr and W. Kurz, Solidification of Peritectic Alloys, *Int. Mater. Rev.*, 1996, **41**, p 129–164. <https://doi.org/10.1179/imr.1996.41.4.129>
29. J.W. Elmer, S.M. Allen, and T.W. Eagar, Microstructural Development During Solidification of Stainless Steel Alloys, *Metall. Trans. A*, 1989, **20**, p 2117–2131. <https://doi.org/10.1007/BF02650298>
30. H.-S. Noh, J.-H. Kang, K.-M. Kim, and S.-J. Kim, Different Effects of Ni and Mn on Thermodynamic and Mechanical Stabilities in Cr-Ni-Mn Austenitic Steels, *Metall. Trans. A*, 2019, **50**, p 616–624. <https://doi.org/10.1007/s11661-018-5042-0>
31. S. Allain, J.-P. Chateau, O. Bouaziz, S. Migot, and N. Guelton, Correlations Between the Calculated Stacking Fault Energy and the Plasticity Mechanisms in Fe–Mn–C Alloys, *Mater. Sci. Eng. A*, 2004, **387–389**, p 158–162. <https://doi.org/10.1016/j.msea.2004.01.059>
32. Q. Chen and B. Sundman, Computation of Partial Equilibrium Solidification with Complete Interstitial and Negligible Substitutional Solute Back Diffusion, *Mater. Trans.*, 2002, **43**, p 551–559. <https://doi.org/10.2320/matertrans.43.551>
33. Fussik, R. Untersuchung der Mikrostrukturellen Stabilität in Relation mit der Wasserstoffversprödung von Austenitischen FeCrNi-Legierungen, 2020
34. A. Schumacher, *Optimierung Mechanischer Strukturen: Grundlagen und Industrielle Anwendungen*, Springer, Berlin, Heidelberg, 2013
35. H.W. King and D.C. Larbalestier, Austenitic Stainless Steels at Cryogenic Temperatures: The Compositional Dependence of the Ms, *Cryogenics*, 1981, **21**, p 521–524. [https://doi.org/10.1016/0011-2275\(81\)90026-6](https://doi.org/10.1016/0011-2275(81)90026-6)
36. J.-H. Kang, H.-S. Noh, K.-M. Kim, S.C. Lee, and S.-J. Kim, Modified Ni Equivalent for Evaluating Hydrogen Susceptibility of Cr-Ni Based Austenitic Stainless Steels, *J. Alloy. Compd.*, 2017, **696**, p 869–874. <https://doi.org/10.1016/j.jallcom.2016.12.061>
37. E. Perteneder and F. Jeglitsch, *Primary and Secondary Microstructure in Austenitic Welding Deposit and its Influence on Hot Cracking*, Riederer, Germany, 1982

Publisher's Note Springer Nature remains neutral with regard to jurisdictional claims in published maps and institutional affiliations.